Carbon 245 (2025) 120830

Contents lists available at ScienceDirect

Carbon

journal homepage: www.elsevier.com/locate/carbon

Highly efficient and cost-effective carbon paper electrode for inverted perovskite solar cells

Joana Príncipe [a], Vera C. M. Duarte [a], Ana M. V. M. Pereira [a], Adélio Mendes [a], Luísa Andrade [a,*]

[a] LEPABE - Laboratory for Process Engineering, Environment, Biotechnology and Energy, ALiCE - Associate Laboratory in Chemical Engineering, Faculty of Engineering, University of Porto, Rua Dr. Roberto Frias, 4200-465, Porto, Portugal

ARTICLE INFO

Keywords:
Back-contact
Carbon electrode
Carbon paper
Inverted perovskite solar cells

ABSTRACT

Perovskite solar cells (PSCs) are among the most promising photovoltaic technologies, with their power conversion efficiency (PCE) rising from 3.8 % in 2009 to 26.95 % in 2025. However, their commercialization remains hindered by challenges such as the high cost of noble metal back-contacts. Finding affordable alternatives for back-contacts is therefore a key research focus. Carbon-based materials have attracted growing interest due to their abundance, low cost, chemical stability, electronic conductivity, sustainability, and suitability for large-scale deposition. In this work, the effective use of carbon paper (CP) as a back-contact in inverted PSCs was demonstrated. To facilitate charge extraction, a thin metal interlayer, consisting of *ca*. 7 nm of gold (Au) or silver (Ag), was introduced between the electron transport layer and the CP. Five different CPs were tested, yielding PCEs of 6.35 % and 8.65 % for devices incorporating 7 nm Au + CP and 7 nm Ag + CP, respectively. To further enhance charge extraction, the impact of a thermally evaporated molybdenum trioxide-doped gold (7 nm Au:MoO_3) was explored, resulting in enhanced interface quality and reduced recombination losses. A champion device with a PCE of 15.6 % was achieved, making one of the highest reported values for carbon-based inverted PSCs.

1. Introduction

According to a recent report from the International Energy Agency, the world's demand for electricity is rising at its fastest rate in years, driven by robust economic development, intense heat waves, and an increased uptake of energy-powered technologies. Simultaneously, renewable energy sources are rapidly expanding, with solar photovoltaic on track to set new records. For the first time, renewables are expected to generate more power than coal in 2025, and solar photovoltaics alone are predicted to supply about half of the rise in global energy demand between 2024 and 2025 [1].

Among all photovoltaic technologies developed to harvest renewable sunlight energy, perovskite solar cells (PSCs) have made the most remarkable progress. The increase in power conversion efficiency (PCE) from 3.8 % in 2009 [2] to 26.95 % in 2025 [3] has made this technology comparable to commercial silicon solar cells. A PSC is a multilayered device composed of a back-contact (BC), an n-type electron transport layer (ETL), a p-type hole transport layer (HTL), and a light-absorbing perovskite active layer, all assembled on a glass substrate coated with a transparent conductive oxide (TCO). Depending on the deposition order of the charge-transporting layers, PSCs can have regular (n-i-p) or inverted (p-i-n) architectures. Perovskite absorbers present several advantageous properties, including high bandgap tunability, long charge carrier diffusion length, high carrier mobility, compatibility with flexible and scalable manufacturing processes, and low production costs [4–6]. However, some challenges remain, including the accelerated degradation of PSCs under real operating conditions (oxygen, moisture, heat, and ultraviolet light), lead toxicity, scaling up manufacturing, and the use of noble metals for BCs [7].

Typically, high-PCE benchmark laboratory cells use noble metals like gold (Au) or silver (Ag) as BCs. However, these materials increase the manufacturing cost of PSCs and may also impact their stability. For instance, Domanski et al. [8] demonstrated that exposing PSCs to temperatures of 70 °C is enough to induce the migration of Au or Ag atoms

* Corresponding author. LEPABE - Laboratory for Process Engineering, Environment, Biotechnology and Energy, ALiCE - Associate Laboratory in Chemical Engineering, Faculty of Engineering, University of Porto, Rua Dr. Roberto Frias, 4200-465, Porto, Portugal
E-mail address: landrade@fe.up.pt (L. Andrade).

https://doi.org/10.1016/j.carbon.2025.120830
Received 29 July 2025; Received in revised form 5 September 2025; Accepted 8 September 2025
Available online 9 September 2025

toward the perovskite layer, which promotes device degradation. Furthermore, ambient conditions may trigger the decomposition of the perovskite, and the out-diffused halides can react with the Ag electrodes, forming silver iodide, which further impacts the overall PSC performance [9,10]. Substituting Au and Ag with other metals, such as aluminum, copper, and chromium (Cr), is encouraged to reduce the overall cost of PSCs. However, exposing these metals to oxygen and/or moisture induces oxidation, diffusion, and reactions with perovskite decomposition products, also leading to degradation [11–14]. Nickel, an earth-abundant and cost-effective material with a work function (WF) comparable to that of Au, can also serve as BC. However, in inverted PSCs, its WF leads to suboptimal band alignment, hindering charge carrier extraction and ultimately reducing key photovoltaic performance parameters [15].

As a result, finding inexpensive alternative materials for the BC remains one of the primary goals for researchers working on PSCs. Carbon-based materials have gained increasing attention due to their abundance, low cost, sustainability, and ease of large-scale deposition. Moreover, their excellent chemical inertness, electronic conductivity, hydrophobic properties, and similar WF to noble metals make carbon materials suitable for BC applications in PSCs [15–19]. Commercial carbon materials are available in many forms, including carbon paste, carbon black, carbon ink, carbon nanotubes, graphene and graphite. These can be deposited using simple techniques such as doctor-blading, printing, spraying, rolling transfer and painting [17,20].

The first report of a PSC with a carbon-based BC was made in 2013 by Ku et al. [21], demonstrating a reasonable PCE value of 6.64 %. Since then, numerous publications on regular PSCs using various forms of carbon materials have been published [22–32]. However, such applications in inverted PSCs are rare. The use of carbon-based materials as BCs in inverted PSCs is limited by: 1) the poor contact between the ETL and BC, 2) mismatching energy level between the carbon WF and the lowest unoccupied molecular orbital (LUMO) of the ETL, and 3) degradation of the ETL and/or perovskite layer due to solvents when carbon pastes are used [15]. Nonetheless, there have been a few reports of carbon-based BCs in inverted PSCs. In 2017, Luo et al. [33] employed a tin oxide (SnO_2)-coated cross-stacked carbon nanotube (SnO_2@CSCNT) film as a cathode for both rigid and flexible substrates. The SnO_2@CSCNT-based PSCs showed enhanced photovoltaic performance compared to pristine CSCNT-based devices, attributed to reduced charge recombination. The rigid and flexible devices achieved PCE values of 14.3 % and 10.5 %, respectively. However, the best performing device presents a very complex structure: fluorine-doped tin oxide (FTO)/nickel oxide (NiO)-perovskite/aluminum (III) oxide (Al_2O_3)--perovskite/SnO_2@CSCNT-perovskite. Jeon et al. [34] also demonstrated that single-walled carbon nanotube (SWNT) films and graphene could be used as bottom electrodes in flexible inverted PSCs. They further reported the use of carbon nanotubes (CNT) as top electrodes, showing that applying [6,6]-phenyl-C61-butyric acid methyl ester (PCBM) solution directly on top of the CNTs improved the interfacial contact and the electron-transporting ability of the devices. It was concluded that PCBM had an n-type doping effect on CNT films, resulting in enhancedconductivity. As a result, a PCE value of 10.5 % was achieved in a device with the structure indium-doped tin oxide (ITO)/poly (3,4-ethylenedioxythiophene):polystyrenesulfonate (PEDOT:PSS)/perovskite/CNT-PCBM. In 2018, Zhou et al. [35] used polyethylenimine (PEI)-modified cross-stacked super-aligned carbon nanotube (CSCNT: PEI) film as BC in inverted PSCs with the structure FTO/NiO_x/perovskite/PCBM/CSCNT:PEI. By modifying CSCNT with 0.5 wt% of PEI, they achieved suitable energy level alignment and improved interfacial charge transfer at the PCBM/CSCNT interface, which resulted in a significant enhancement in photovoltaic performance, with a champion PCE of 10.8 %.

Despite these promising results, all these studies employed complex and expensive procedures to fabricate the CNT films, including chemical vapor deposition, annealing processes, and cross-stacking of CNTs. These methods are not suitable for large-scale production. In 2020, Babu et al. [36] successfully used commercial carbon paste as a BC in inverted PSCs. After optimizing thickness and annealing conditions, they achieved a device structure of polyethylene terephthalate-indium zinc oxide (PET-IZO)/poly[bis(4-phenyl)(2,4,6-trimethylphenyl)amine (PTAA)/-perovskite/PCBM/Cr/carbon. They tested various buffer layers to act as a mechanical shield, protecting the underlying layers from damage caused by carbon film deposition. They found that a thin layer of thermally evaporated Cr between the ETL and carbon electrode enabled efficient electron collection. The champion Cr/carbon-based device reached 15.18 % of PCE. Following the same strategy, Lukas et al. [37] introduced a buffer layer of atomic layer deposited SnO_2 to prevent the damage of the ETL induced by the carbon paste solvents. Furthermore, to enhance electrical contact between the SnO_2 and the carbon electrode, an interlayer of PEDOT:PSS was also considered to suppress the formation of an energy barrier, reaching a maximum PCE of 16.1 %.

While carbon pastes simplify BC fabrication, some challenges remain, such as solvents migration from the carbon pastes into the inner layers of the device, leading to degradation. Additionally, as demonstrated by Babu et al. [36] and Lukas et al. [37], an interlayer is always required to shield the underlying layers from damage during carbon film deposition. An alternative carbon material with high conductivity is carbon papers (CPs), originally developed as gas diffusion layers for proton-exchange membrane fuel cells and later adapted as BCs in mesoporous regular PSCs [38,39]. However, to the best of the authors' knowledge, CPs have never been used as BCs in inverted PSCs. Their application is straightforward, as they can be used as received and simply placed on the device surface, making them an attractive option for large-scale PSC production.

In this work, the effective use of carbon paper as a BC in inverted PSCs (electron collection at the BC) was demonstrated. This was achieved by introducing a thin layer of metal (7 nm) between the ETL and the carbon electrode interface, enabling ohmic contact between these layers and facilitating efficient electron collection. A combination of five different carbon papers with metal interlayers of gold, silver, and molybdenum trioxide-doped gold (Au:MoO_3) was tested, and the PSC device's photovoltaic performance was evaluated. As a result, a champion inverted PSC with a PCE of 15.6 % was obtained for a device with a 7 nm film of Au:MoO_3 + CP as BC. Moreover, this strategy shows promise for large-scale and/or flexible inverted PSC production.

2. Experimental

2.1. Materials

The FTO-coated glass substrates (7 $\Omega \cdot sq^{-1}$) were purchased from Greatcell Solar Materials. PTAA and PCBM were purchased from Ossila. Bathocuproine (BCP) was purchased from Sigma-Aldrich. The 4-fluorophenethylammonium iodide compound (F-PEAI) was purchased from TCI Europe N.V. Perovskite films were fabricated using lead iodide (PbI_2) and lead bromide ($PbBr_2$) from TCI Europe N.V., cesium iodide (CsI) from Sigma-Aldrich, formamidinium iodide (FAI) and methylammonium bromide (MABr) from Greatcell Solar Materials. Acetone and 2-propanol were purchased from VWR. Anhydrous solvents (2-propanol, chlorobenzene, dimethyl sulfoxide (DMSO), *N*,*N*-dimethylformamide (DMF) and toluene) were purchased from Sigma-Aldrich. Ag, Au and molybdenum oxide (MoO_x) pellets were purchased from Photon Export.

Five different commercially available carbon papers were tested: LT2400W named here as CP1, was acquired from ELAT®, H14C10, H23C7 and H24C5, named here as CP2, CP3 and CP4, were acquired from Freudenberg group, and 28BC, named here as CP5, was acquired from SIGRACET®. Table S1 in the Supplementary Information presents the properties of the five carbon papers used in this study.

2.2. PSC fabrication

The procedure used to fabricate the inverted PSCs was based on methods reported elsewhere [40]. FTO-glass substrates were washed with a 10 % Hellmanex aqueous solution followed by distilled water. The glass substrates were then sequentially cleaned by ultra-sonication with acetone and 2-propanol for 15 min in each solvent. The cleaned substrates were dried with a nitrogen flow and treated with oxygen plasma at 100 mW for 10 min before the deposition of active layers. All depositions, except for the BC layer, were performed using a spin-coater inside a N_2-filled glovebox.

First, the PTAA layer (1.5 mg mL^{-1} in toluene) was spin-coated at 2000 rpm for 40 s and then annealed at 100 °C for 10 min. After the annealing step, the samples were washed with a 5 mg mL^{-1} solution of F-PEAI in DMF by spin-coating at 4000 rpm for 30 s. Next, the perovskite film was deposited. A perovskite precursor solution of 1.2 M $Cs_{0.05}(FA_{0.85}MA_{0.15})_{0.95}Pb(I_{0.85}Br_{0.15})_3$ was prepared by mixing different cations (Pb, Cs, FA, and MA) and halides (I and Br) in a solvent mixture of DMF/DMSO 4:1, using an excess of PbI_2 of 10 %. The perovskite layer was fabricated using a two-step spin-coating procedure: first at 1000 rpm for 12 s and then at 5000 rpm for 27 s. At 21 s during the second spin-coating step, the antisolvent (a 0.125 mg mL^{-1} solution of F-PEAI in a mixture of chlorobenzene/2-propanol 9:1) was dripped onto the spinning substrate. Subsequently, the samples were annealed at 100 °C for 30 min. After the annealing process, the substrates were cooled, and a 20 mg mL^{-1} PCBM solution in chlorobenzene was spin-coated onto the perovskite layer at 2000 rpm for 30 s (with a ramping speed of 1000 rpm s^{-1}). The PCBM films were then annealed at 100 °C for 10 min. Next, a 0.5 mg mL^{-1} BCP solution in 2-propanol was spin-coated at 4000 rpm for 30 s (with a ramping speed of 1000 rpm s^{-1}) as the buffer layer. For the carbon-based devices, different metal interlayers made of Ag, Au, and Au:MoO_3 were thermally evaporated under high vacuum ($<3 \times 10^{-6}$ mbar) on top of the BCP layer. PSCs with 80 nm of Ag and Au were also prepared as references. The deposition of all these layers was carried out applying the following deposition rates: 1) 0.01 nm·s^{-1} until 4 nm, 2) 0.04 nm·s^{-1} until 7 nm, 3) 0.07 nm·s^{-1} until 10 nm, 4) 0.10 nm·s^{-1} until 20 nm, 5) 0.13 nm·s^{-1} until 30 nm, 6) 0.15 nm·s^{-1} until 50 nm, and 7) 0.20 nm·s^{-1} until 80 nm. After deposition was complete, the vacuum was released, and the PSCs were removed to characterization.

2.3. Dummy cells fabrication

The preparation of dummy cells was similar to that of the complete inverted PSCs, but only some of the layers were deposited: FTO/PCBM/BCP/BC.

2.4. Characterization of films and devices

The PSCs were first characterized with only the metal interlayer (Fig. 1a) to assess the main photovoltaic parameters. Then, the carbon papers were randomly placed on top of the stacked device, and the devices were characterized again (Fig. 1b). Several batches of 16 cells were prepared to assess reproducibility, and the results were statistically analyzed.

The photocurrent-voltage (*J-V*) characteristics curves of the PSCs were obtained by applying an external potential load and measuring the generated photocurrent using a Zennium workstation (Zahner Elektrik, Germany) controlled by the Thales software package (Thales XT 5.1.4). The measurements were performed under AM 1.5 irradiation at 100 mW cm^{-2} (1 sun), supplied by a solar simulator (150 W Oriel class A). The simulator was calibrated using a single-crystal Si photodiode (Newport, USA). The scan speed and voltage step used were 20 mV s^{-1} and 10 mV, respectively. The devices were characterized immediately after their preparation, at room temperature and in ambient air. The active area of the solar cells was defined by a shadowing black mask with an aperture area of 0.196 cm^2. Cyclic voltammetry was performed on the dummy cells. These measurements were carried out by applying an external potential load and measuring the generated photocurrent using the same Zennium workstation (Zahner Elektrik, Germany), controlled by the Thales software package (Thales XT 5.1.4). The work functions of metallic BCs and carbon papers were determined using an ultra-high vacuum Kelvin Probe (KPTechnology, Series 10) at ambient pressure. X-ray photoelectron spectroscopy (XPS) was performed using a KRATOS Axis Ultra HAS-Vision X-ray photoelectron spectrometer with a monochromatic X-ray source (Al). Scanning electron microscopy (SEM) characterization was carried out using a Phenom XL desktop SEM. Digital microscope images were obtained using an achromatic lens and CMOS image sensor. The surface morphology of the samples was analyzed using an atomic force microscopy (AFM) (MFD-3D Infinity, Oxford Instruments). Electrochemical impedance spectroscopy (EIS) was conducted with a potentiostat (Metrohm Autolab, Netherlands) in the frequency range of 100 kHz to 0.1 Hz, with an AC modulation signal of 10 mV. EIS measurements were performed in dark conditions under different applied potentials, ranging from open circuit potential to 0 V, with 50 mV steps.

3. Results and discussion

Carbon papers are carbon-carbon composites consisting of carbon fibers held together by a carbon matrix, typically formed after heat treatment. CPs can be made hydrophobic by adding PTFE and can feature a microporous layer to minimize contact resistance.

To identify the best-performing CP, each was tested by evaluating the current-voltage (*I–V*) characteristics of dummy cells with the structure FTO/PCBM/BCP/CP. Additionally, dummy cells with the structure FTO/PCBM/BCP/metal were tested for Ag and Au, both with a thickness of 80 nm. The results, shown in Fig. 2, revealed that the Ag and Au devices exhibited linear *I–V* characteristics between −1 V and 1 V, indicating that metals formed an ohmic contact with the PCBM/BCP layer, as expected. In contrast, the CPs showed slightly curved *I–V* characteristics (non-ohmic contact) between −1 V and 1 V, suggesting

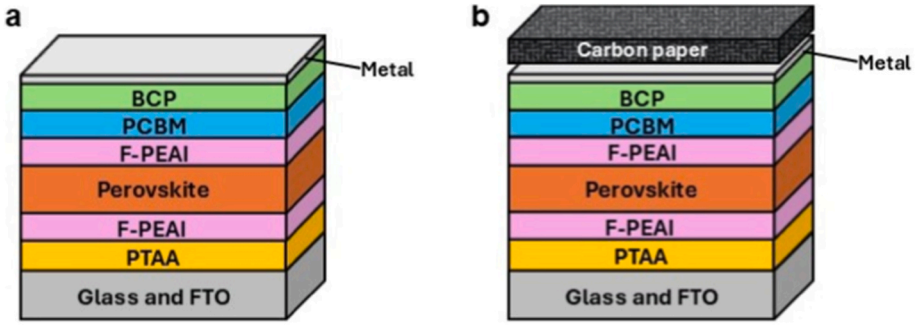

Fig. 1. – PSC architecture used in this work a) without and b) with the carbon paper as back-contact.

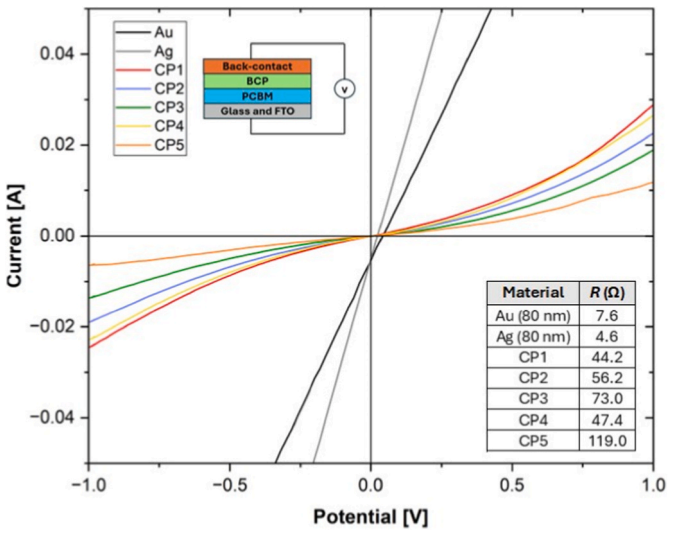

Fig. 2. – *I–V* curves of dummy devices (FTO/PCBM/BCP/BC). Insets: device scheme and slope values (*R*) of the *I–V* curves.

charge accumulation at the PCBM/BCP and CP interface. Among the carbon papers, CP1 exhibited the lowest ohmic resistance (highest slope), followed by CP4, CP2, CP5 and CP3. Due to its high resistance, CP3 and CP5 were discarded at this stage.

Complete inverted PSC devices with carbon papers as BC were fabricated following the procedure described in section 2.2. It was observed that charge extraction was not possible when using only carbon paper as BC, resulting in near-zero device performance. Previous studies suggest that two main factors limit the use of carbon-based materials as BC in inverted PSCs: 1) poor contact at the PCBM/carbon electrode interface, and 2) energy level mismatch between the LUMO level of PCBM and the WF of the carbon-based electrodes [35,37,41]. To investigate the latter, the WF of Ag, Au, and CPs was measured. The values obtained were −4.61 eV for CP1, -4.68 eV for CP2, -4.73 eV for CP4, -4.71 eV for Ag, and −4.79 eV for Au. The observed differences between the WF of CPs and noble metals are not sufficient to create a potential energy barrier for charge carriers. Therefore, the poor device performance may be attributed to the high ohmic resistance at the PCBM/carbon interface, hindering charge collection. To address this issue, an interlayer was introduced between the ETL and CP. Different interlayer thicknesses, ranging from 4 nm to 15 nm, were tested using either Au or Ag (Table 1 and Fig. S1–S11 in Supplementary Information). Analyzing all these results, it can be concluded that the optimal thickness of the metal interlayer should be determined based on the relative performance improvement achieved when a CP is added. In this study, a gold thickness of 7 nm was found to allow a 28 % PCE improvement, while for 15 nm only 1.5 % is reached. This behavior can be explained by the morphology of the metal layer: at 7 nm, the interlayer forms sharp peaks that establish discrete contact points with the CP, resulting in low electrical resistance. For thicknesses below 7 nm, there is insufficient material to create effective contact points. Conversely, at thicknesses well above 7 nm, the metal tends to form a continuous thin film, supporting efficient charge extraction alone; thus, the addition of CP does not provide a significant improvement in photovoltaic performance compared to thinner interlayers. This suggests that CPs can effectively serve as electrodes in these devices. The metal interlayer appears to play a crucial role in facilitating efficient electron transfer to the CP, as indicated by enhanced performance. However, despite the improvements, the high resistance at the ETL/CP interface limits the overall PCE of PSC devices, preventing this approach from being competitive with previously reported carbon-based BCs. Consequently, an alternative strategy was explored to further optimize the device performance.

Table 1
Results of open-circuit voltage (V_{oc}), short-circuit current (J_{sc}), fill factor (FF) and PCE of the best-performing PSCs under study, with and without CPs, under 1 sun (100 mW cm^{-2}, AM 1.5 G, room temperature). In parathesis, the average values and the standard deviation are presented.

	V_{oc} [V]	J_{sc} [mA · cm^{-2}]	FF	PCE [%]
Au (80 nm)	**1.08** (1.09 ± 0.0163)	**24.0** (22.7 ± 0.693)	**0.773** (0.733 ± 0.0375)	**20.0** (18.1 ± 0.998)
Au interlayer (7 nm)	**1.01** (0.981 ± 0.0485)	**12.8** (10.7 ± 1.61)	**0.358** (0.325 ± 0.0330)	**4.59** (3.45 ± 0.795)
Au interlayer (7 nm) + CP (Best-performing devices)	**1.04** (0.989 ± 0.0620)	**14.9** (13.4 ± 1.23)	**0.408** (0.386 ± 0.0296)	**6.35** (5.11 ± 0.837)
Ag (80 nm)	**1.06** (1.07 ± 0.0246)	**23.5** (22.8 ± 1.13)	**0.759** (0.687 ± 0.0346)	**18.8** (16.7 ± 1.01)
Ag interlayer (7 nm)	**1.03** (1.02 ± 0.0240)	**13.9** (12.5 ± 1.23)	**0.440** (0.414 ± 0.0752)	**6.26** (5.29 ± 0.964)
Ag interlayer (7 nm) + CP (Best-performing devices)	**1.05** (1.04 ± 0.0244)	**16.2** (15.4 ± 0.570)	**0.512** (0.476 ± 0.0251)	**8.65** (7.63 ± 0.558)

Molybdenum oxide has emerged as a promising material for enhancing the performance of carbon-based electrodes in inverted PSCs. Jeon et al. [42] demonstrated the use of MoO_3 to dope a carbon-based bottom electrode, leveraging its well-known stability and compatibility with carbon nanotubes and graphene electrodes [43–45]. Furthermore, MoO_x has also been widely explored in regular PSCs, both as a standalone BC material [46] and in combination with metals such as aluminum [47] or gold [48], as well as an interlayer between the HTL/BC interface [49,50]. Additionally, a recent work of Jiang et al. [51] highlighted the effectiveness of a magnetron-sputtered molybdenum rear electrode coupled with a bismuth buffer layer prepared by thermal evaporation as a bilayer electrode in inverted PSCs. Despite achieving a notable PCE this approach is not suitable for flexible substrates nor for large-scale production due to the deposition methods selected and the high temperatures reached during the deposition of the active layers. Moreover, some literature suggests that bismuth's life cycle impact may be worse than lead in certain categories [52]. Nevertheless, the study proposes that molybdenum not only improves charge extraction but also enhances the overall device stability, making it a key material in the development of high-performance carbon-based back-contacts.

Therefore, in this work, molybdenum oxide was used as a doping agent for the metal back-contact. PSC devices with a thin 7 nm film of thermally co-deposited Au:MoO_x were fabricated. Films of Ag:MoO_x were not successfully deposited in our laboratory due to equipment limitations and the proximity of the melting points of these materials. XPS analysis was employed to investigate the surface chemical composition and elemental chemical states of the deposited interlayer (Fig. 3). The survey spectrum reveals the presence of Mo, O, and Au elements on the device surface (Fig. 3a). The Mo 3d spectrum (Fig. 3b) shows the 5/2-3/2 spin-orbit doublet at 233.2 eV (Mo $3d_{5/2}$) and 236.3 eV (Mo $3d_{3/2}$), corresponding to Mo^{6+} in the MoO_3 state. Additionally, the O 1s spectrum (Fig. 3c) displays a peak at 531.3 eV, attributed to O^{2-} ions in the oxide [53,54]. The O/Mo atomic ratio was determined to be 3.4, which is close to the theoretical value of 3.0, confirming the formation of MoO_3. The Au 4f spectrum (Fig. 3d) shows two peaks at binding energies of 84.5 eV and 88.2 eV, with a 3.7 eV separation between the spin-orbit components, corresponding to elemental gold [55,56]. The atomic concentration of Au in the Au:MoO_3 composite film was calculated to be 1.3. Additionally, the WF of the Au:MoO_3 composite film was measured to be −4.57 eV, matching the energetic levels of the CPs, as can be seen in Fig. 4.

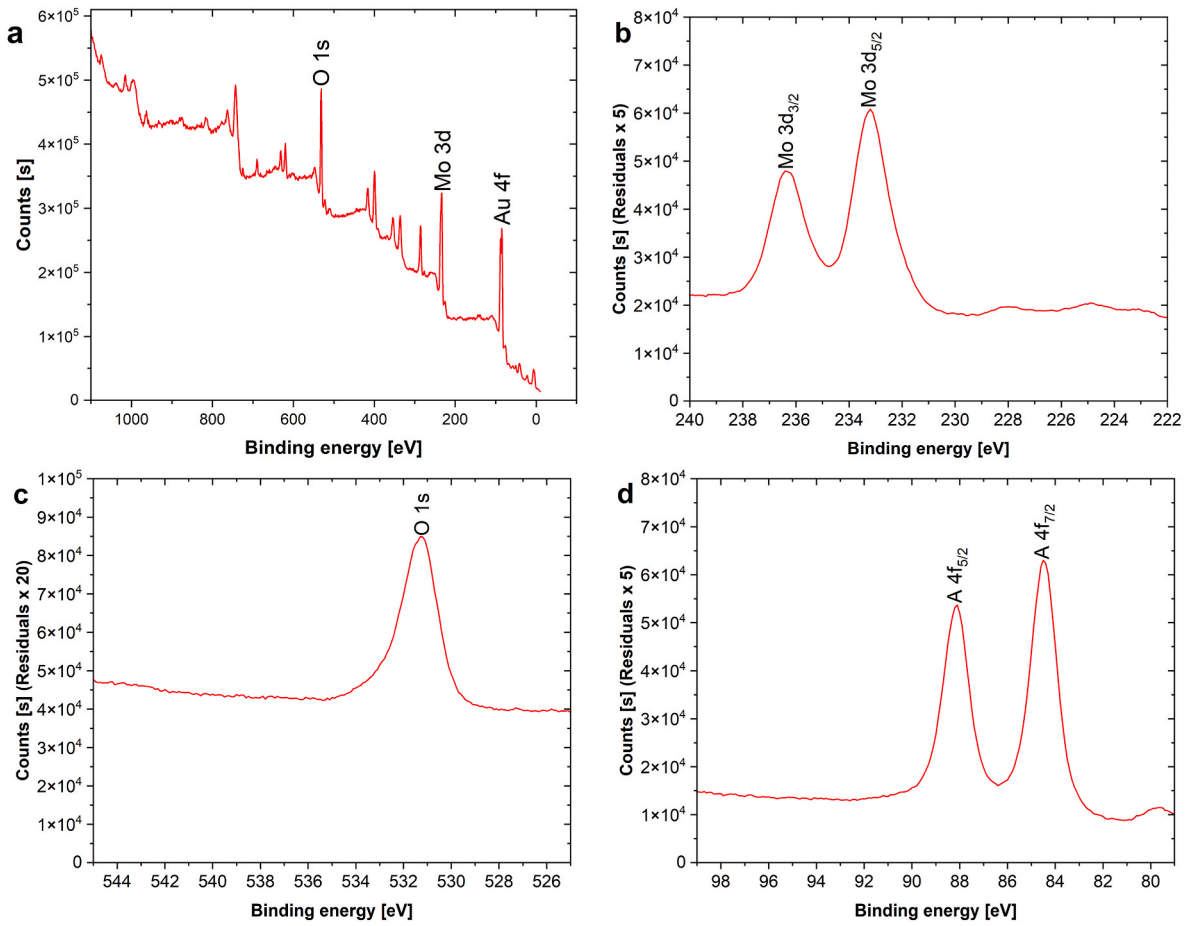

Fig. 3. – a) XPS survey spectrum of the Au:MoO_3 film deposited as interlayer; b) detail of the Mo 3d region; c) detail of the O 1s region; and d) detail of the Au 4f region.

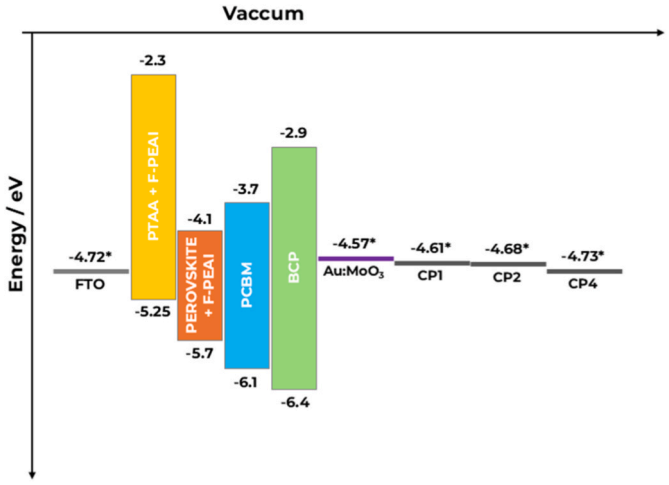

Fig. 4. – Energy diagram of PSC materials and carbon papers. The energy levels marked with * were measured by the authors, while the others were taken from the literature [57–60].

Table 2 presents the best-performing devices and the statistical analysis of the results obtained from the inverted PSCs with 7 nm Au:MoO_3 interlayer, with and without CPs. From this table, it is clear that the addition of the thin interlayer combined with the CPs improved the photovoltaic performance of the devices. The best performance was achieved with the Au:MoO_3 + CP1 combination, resulting in a PCE of 15.6 %. The corresponding *J-V* characteristic curves are shown in Fig. 5. Additionally, Table 2 shows that, although the CPs were used randomly, CP1 delivered the best performance compared to CP2 and CP4. Furthermore, during the characterization of the PSCs, it was also observed that CPs can be reused multiple times without compromising their performance. This reusability further motivates the use of CPs as BCs, improving the sustainability of PSCs and reducing their manufacturing costs.

Table 2
– Solar cell parameters for the best-performing PSCs with 7 nm Au:MoO_3 interlayer, with and without CPs, under 1 sun (100 mW cm^{-2}, AM 1.5 G, room temperature). In parathesis, the average values and the standard deviation are presented.

	V_{oc} [V]	J_{sc} [mA · cm^{-2}]	FF	PCE [%]
Au:MoO_3 interlayer (7 nm)	**1.07** (1.06 ± 0.0333)	**9.04** (6.24 ± 3.05)	**0.270** (0.468 ± 0.360)	**2.61** (2.38 ± 0.479)
Au:MoO_3 interlayer (7 nm) + CP1	**1.12** (1.12 ± 0.00577)	**21.6** (20.4 ± 1.07)	**0.646** (0.644 ± 0.00667)	**15.6** (14.7 ± 0.801)
Au:MoO_3 interlayer (7 nm) + CP2	**1.12** (1.11 ± 0.00878)	**18.7** (17.7 ± 1.00)	**0.527** (0.496 ± 0.0575)	**11.0** (9.82 ± 1.67)
Au:MoO_3 interlayer (7 nm) + CP4	**1.09** (1.09 ± 0.0188)	**18.5** (18.4 ± 0.568)	**0.497** (0.458 ± 0.0357)	**10.1** (9.20 ± 0.970)

Fig. 6 shows SEM and AFM images of PSC devices with 7 nm Au and 7 nm Au:MoO_3 interlayers. The SEM images reveal that the 7 nm Au

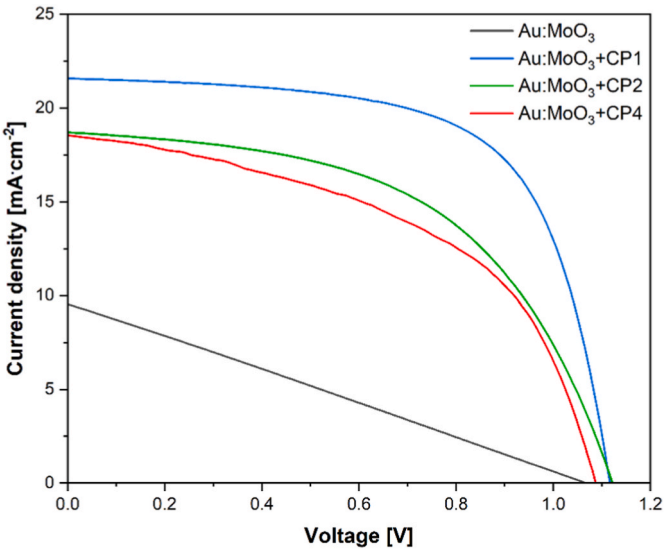

Fig. 5. – *J-V* characteristic curves for the champion PSC devices with 7 nm Au:MoO_3 interlayer, with and without the CPs, under 1 sun (100 mW cm^{-2}, AM 1.5 G, room temperature).

interlayer consists of discrete gold spots (Fig. 6a). Additionally, the surface roughness of the 7 nm Au sample (Fig. 6c) is higher than that of the 7 nm Au:MoO_3 interlayer, as the thin Au interlayer does not fully cover the PSC surface. In contrast, the SEM and AFM images of the Au:MoO_3 interlayer (Fig. 6b and d, respectively) show a more uniform and smoother film, with Au more evenly distributed across the surface rather than forming agglomerated spots, resulting in reduced surface roughness. It is hypothesized that the improved surface coverage of the Au:MoO_3 interlayer reduces charge recombination at the PCBM/BC interface. The smoother, more continuous surface likely minimizes defects and irregularities at the interface, which are commonly associated with recombination losses. This enhanced interface quality, combined with more efficient charge extraction, contributes to the higher photovoltaic performance observed with the Au:MoO_3 interlayer compared to the Au-only interlayer.

To further investigate the charge transfer, EIS analysis was performed on the complete devices with 7 nm Au:MoO_3 + CPs as BC. The interfacial charge transfer and interfacial transport resistance at the BC were modeled as a parallel constant phase element (CPE) and a resistor element circuit, as illustrated in Fig. 7 [39]. The parameters of this model for the characterized devices are provided in Table 3. Consistent with the results in Table 2, CP1 exhibits the lowest interfacial electric resistance, followed by CP2 and CP4. This can be attributed to the well-organized and dense matrix of carbon fibers beneath the microporous layer in CP1, as shown in Fig. 8a–d; comparing CP2 and CP4, both present similar fiber organization. However, the lower density of carbon fibers and the presence of voids between them may explain why CP2 (Fig. 8g–h) outperforms CP4 (Fig. 8k–l), despite the similar organizational structure.

As previously mentioned, in addition to cost considerations, the sustainability of materials used in PSC is crucial. Equally important is understanding the environmental impact of these materials. This can be effectively evaluated using the life cycle assessment (LCA) methodology, which is currently the most prevalent method for assessing the environmental impacts of a product across its entire life cycle [61,62]. So, a LCA study was conducted to understand the environmental impacts of the novel BC under study: 7 nm Au:MoO_3 + CP. Moreover, the environmental performance of the noble metal-based BCs with 80 nm Ag and 80 nm Au was also assessed. A "cradle-to-gate" approach was employed, focusing exclusively on the manufacturing phase of the BCs. Since this analysis concentrates solely on the production stage of the BC, the active

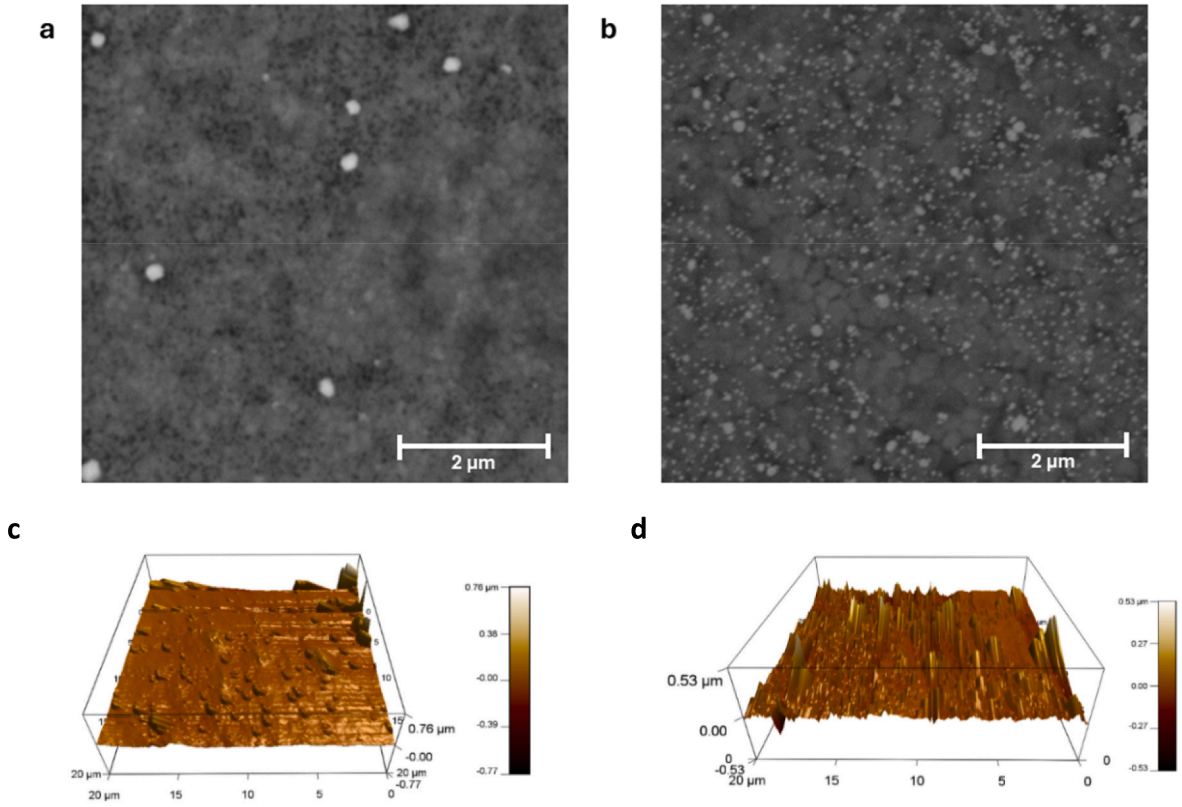

Fig. 6. – SEM and AFM surface morphology analysis: SEM top-view images of a) 7 nm Au interlayer, b) 7 nm Au:MoO_3 interlayer (the scale bar is 2 µm for both images); AFM images of c) 7 nm Au interlayer and d) 7 nm Au:MoO_3 interlayer.

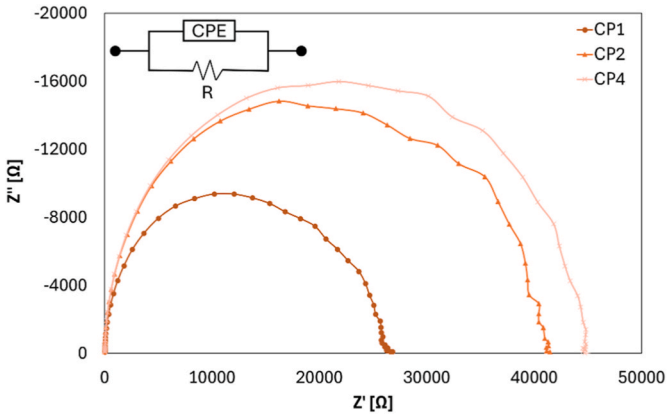

Fig. 7. – Nyquist plots for PSCs with the combined 7 nm Au:MoO_3 interlayer + CPs. Inset: equivalent circuit.

Table 3
– Fitting results of the RC impedance model used to characterize the systems 7 nm Au:MoO_3 interlayer + CPs.

Carbon paper	*R* [kΩ]	CPE [F]	n
CP1	24.10	2.914×10^{-8}	0.95
CP2	37.75	2.718×10^{-8}	0.95
CP4	41.08	2.867×10^{-8}	0.95

area of a PSC (2.88 cm^2) was selected as the functional unit (FU). Choosing a unit area as the FU enables a more objective and direct comparison between the different BCs, independent of their efficiency or power output.

The ReCiPe 2016 midpoint method with an egalitarian perspective was used to evaluate environmental impacts [63]. The egalitarian perspective was chosen for its precautionary nature, as it considers all potential environmental impact pathways. This perspective is also considered the most conservative, or pessimistic, in its assessment [64]. The ReCiPe 2016 method evaluates the following 18 potential environmental impact categories: Global Warming (GW, kg CO_2 eq.), Stratospheric Ozone Depletion (SOD, kg CFC-11 eq.), Ionizing Radiation (IR, kBq Co-60 eq.), Ozone Formation Human Health (OFHH, kg NOx eq.), Fine Particulate Matter Formation (FPMF, kg PM2.5 eq.), Ozone Formation Terrestrial Ecosystems (OFTE, kg NOx eq.), Terrestrial Acidification (TA, kg SO_2 eq.), Freshwater Eutrophication (FETP, kg P eq.), Marine Eutrophication (METP, kg N eq.), Terrestrial Ecotoxicity (TECT, kg 1,4-DCB), Freshwater Ecotoxicity (FECT, kg 1,4-DCB), Marine Ecotoxicity (MECT, kg 1,4-DCB), Human Carcinogenic Toxicity (HCT, kg 1,4-DCB), Human Non-Carcinogenic Toxicity (HNCT, kg 1,4-DCB), Land use (LU, m^2a crop eq.), Mineral Resource Scarcity (MRS, kg CU eq.), Fossil Resource Scarcity (FRS, kg oil eq.), and Water Consumption (WC, m^3).

Since environmental impacts are attributed to the FU, this is an attributive LCA study designed to facilitate direct comparison between the BCs. Portuguese and/or European conditions were considered wherever possible. The life cycle inventory (LCI) relies on primary data

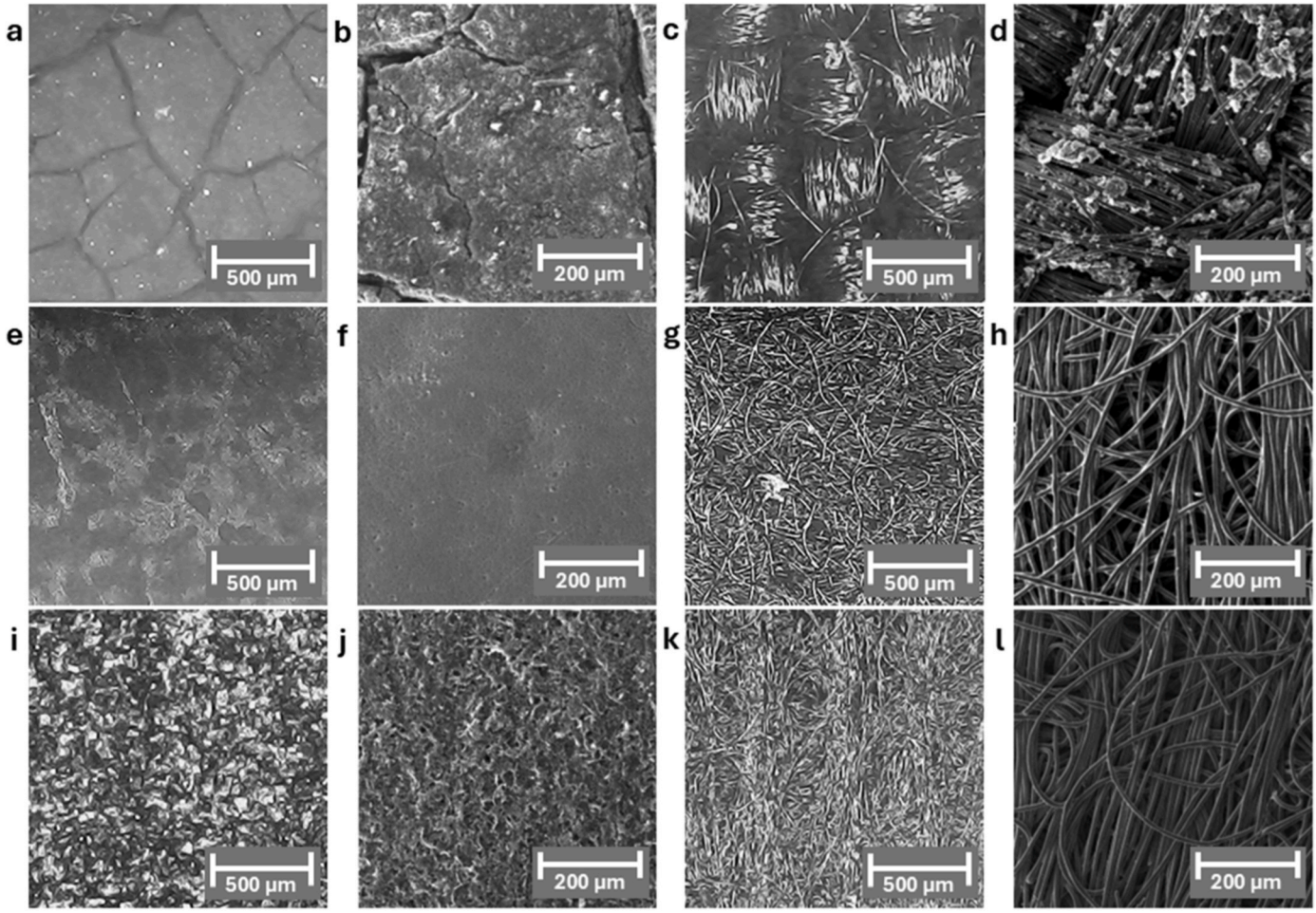

Fig. 8. – Digital microscope and SEM images of CPs surfaces: a), b) microporous layer and c), d) carbon fibers of CP1; e), f) microporous layer and g), h) carbon fibers of CP2; and i), j) microporous layer and k), l) carbon fibers of CP4.

obtained from laboratory-scale manufacturing of the BCs. The background processes include the production and transportation of raw materials to the production site, as well as the generation of the consumed energy, considering the distance from the supplier to the laboratory. For silver, gold, and molybdenum, LCI data were sourced from the Ecoinvent database v3.9.1, accessed via SimaPro™ v9.5.0.1 software (PhD version). For the carbon paper, data were gathered from the literature, with calculations performed to adjust the data to the FU chosen for this study. Material and energy inventory data for the manufacturing of BCs are provided in Table 4.

Fig. 9 presents the environmental impact results for the various BCs under study. The absolute values are provided in Table S3 of the Supplementary Information. As expected, the 80 nm Au BC exhibits the highest environmental impact across all categories. Depending on the impact category, the 80 nm Ag may either exceed or fall below the impacts associated with the 7 nm Au:MoO_3 BC. In particular, for the categories MRS, HNCT, MECT, and FECT, the 80 nm Ag BC demonstrates lower environmental impacts compared to the 7 nm Au:MoO_3. This trend can be attributed to the comparatively higher ecological burden of gold extraction, which involves the use of toxic substances such as mercury and cyanide, as well as significantly greater energy requirements than silver mining. Conversely, for the remaining categories, the 7 nm Au:MoO_3 BC presents a lower environmental impact than the 80 nm Ag BC. Notably, in the global warming category, which is closely associated with carbon emissions from energy consumption, the 7 nm Au:MoO_3 BC reports a substantially lower impact of 0.24 kg CO_2 eq., compared to 1.87 kg CO_2 eq. for the 80 nm Ag BC.

4. Conclusions

Replacing noble metal-based back-contacts in PSCs with low-cost alternative materials is essential for reducing production costs and enhancing the competitiveness of PSC technology against commercially available options. Carbon-based materials, due to their abundance, low cost, and sustainability, are gaining increasing attention in this context. This study demonstrates that carbon papers made from carbon fibers can serve as efficient back-contacts in inverted PSCs for electron collection at the BC. To optimize performance, a thin 7 nm metal interlayer was introduced between the ETL and the carbon electrode. The best-performing device with 7 nm of Au + CP interlayer achieved a PCE of 6.35 %, while the device with a 7 nm of Ag + CP interlayer reached a PCE of 8.65 %. Additionally, it was found that a 7 nm thermally co-deposited Au:MoO_3 interlayer significantly improved charge extraction, resulting in even higher-performing devices. The champion device with CP1 achieved an impressive 15.6 % PCE, one of the highest reported values for carbon-based inverted PSCs. As previously mentioned, the carbon papers used in this work exhibit excellent chemical inertness and hydrophobicity, which are crucial in extreme conditions of moisture and temperature. In addition to being carbon-based, most CPs undergo hydrophobic treatment, further enhancing their suitability as BCs for achieving long-term stable PSCs. The flexibility of CPs and the ability to pattern them into various shapes are other notable features when considering large-scale and/or flexible PSC production.

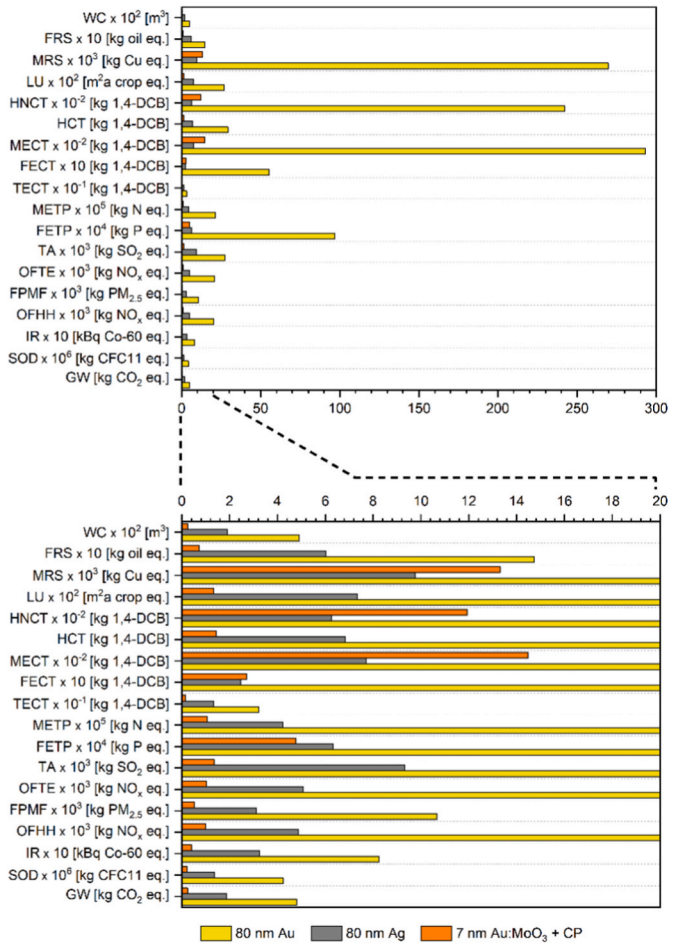

Fig. 9. – Comparison of the life cycle impact assessment results of different back-contacts (impact per cm^2).

Table 4
– Life cycle inventory results for the production of the different back-contacts.

Back-contact	Material/ Equipment	Amount	Unit	Comments
7 nm Au: MoO_3 + CP	Au	1.23×10^{-3}	g	Amount of gold deposited in 1 PSC. LCI data source obtained from the Ecoinvent v3.9.1.
	MoO_3	4.07×10^{-4}	g	Amount of molybdenum deposited in 1 PSC. LCI data source obtained from the Ecoinvent v3.9.1.
	Thermal evaporation (Power: 2300 W)	4.60	kWh	Energy consumed by the equipment during 7200 s.
	CP	1.73×10^{-2}	g	Amount of carbon paper used in 1 PSC. LCI data source obtained from Ref. [65].
80 nm Ag	Ag	2.50×10^{-2}	g	Amount of silver deposited in 1 PSC. LCI data source obtained from the Ecoinvent v3.9.1.
	Thermal evaporation (Power: 2300 W)	5.75	kWh	Energy consumed by the equipment during 9000 s.
80 nm Au	Au	5.00×10^{-2}	g	Amount of gold deposited in 1 PSC. LCI data source obtained from the Ecoinvent v3.9.1.
	Thermal evaporation (Power: 2300 W)	8.05	kWh	Energy consumed by the equipment during 12 600 s.

CRediT authorship contribution statement

Joana Príncipe: Writing – original draft, Visualization, Methodology, Investigation, Formal analysis, Data curation, Conceptualization. **Vera C. M. Duarte:** Writing – review & editing, Visualization, Validation, Supervision, Methodology, Investigation, Conceptualization. **Ana M. V. M. Pereira:** Investigation, Formal analysis. **Adélio Mendes:** Writing – review & editing, Supervision, Resources. **Luísa Andrade:** Writing – review & editing, Validation, Supervision, Resources, Methodology, Funding acquisition, Conceptualization.

Declaration of competing interest

The authors declare that they have no known competing financial interests or personal relationships that could have appeared to influence the work reported in this paper.

Acknowledgments

This research work was supported by the doctoral grant (PRT/BD/152838/2021) of Joana Príncipe financed by the Portuguese Foundation for Science and Technology (FCT) and with funds from the State Budget, under the MIT Portugal Program (DOI: PRT/BD/152838/2021" title = "https://doi.org/10.54499/PRT/BD/152838/2021>https://doi.org/10.54499/PRT/BD/152838/2021). This work is financially supported by: national funds through the FCT/MCTES (PIDDAC), under the project PTDC/EQU-EQU/4193/2021 (DOI: 10.54499/PTDC/EQU-EQU/4193/2021); national funds through FCT/MCTES (PIDDAC): LEPABE, UIDB/00511/2020 (DOI: 10.54499/UIDB/00511/2020) and UIDP/00511/2020 (DOI: 10.54499/UIDP/00511/2020) and ALiCE, LA/P/0045/2020 (DOI: 10.54499/LA/P/0045/2020). Vera C. M. Duarte and Ana M. V. M. Pereira thanks the support of Agenda "H2Driven Green Agenda", nr. C644923817-00000037, investment project nr. 50, financed by the Recovery and Resilience Plan (PRR) and by European Union - NextGeneration EU.

Appendix A. Supplementary data

Supplementary data to this article can be found online at https://doi.org/10.1016/j.carbon.2025.120830.

References

[1] Internation Energy Agency *Electricity Mid-year Update - July 2024*, 2024.
[2] A. Kojima, K. Teshima, Y. Shirai, T. Miyasaka, Organometal halide perovskites as visible-light sensitizers for photovoltaic cells, J. Am. Chem. Soc. 131 (2009) 6050–6051, https://doi.org/10.1021/ja809598r.
[3] NREL, Best research-cell efficiency chart. https://www.nrel.gov/pv/cell-efficiency.html, 2025. March 2025.
[4] Z. Li, T.R. Klein, D.H. Kim, M.J. Yang, J.J. Berry, M.F.A.M. van Hest, et al., Scalable fabrication of perovskite solar cells, Nat. Rev. Mater. 3 (2018) 18017, https://doi.org/10.1038/natrevmats.2018.17.
[5] Y.F. Gu, H.J. Du, N.N. Li, L. Yang, C.Y. Zhou, Effect of carrier mobility on performance of perovskite solar cells, Chin. Phys. B 28 (2019) 048802, https://doi.org/10.1088/1674-1056/28/4/048802.
[6] M.H. Miah, M.U. Khandaker, M.B. Rahman, M. Nur-E-Alam, M.A. Islam, Band gap tuning of perovskite solar cells for enhancing the efficiency and stability: issues and prospects, RSC Adv. 14 (2024) 15876–15906, https://doi.org/10.1039/d4ra01640h.
[7] J. Príncipe, V.C.M. Duarte, L. Andrade, Inverted perovskite solar cells: the emergence of a highly stable and efficient architecture, Energy Technol-Ger (10) (2022) 2100952, https://doi.org/10.1002/ente.202100952.
[8] K. Domanski, J.P. Correa-Baena, N. Mine, M.K. Nazeeruddin, A. Abate, M. Saliba, et al., Not all that glitters is gold: metal-migration-induced degradation in perovskite solar cells, ACS Nano 10 (2016) 6306–6314, https://doi.org/10.1021/acsnano.6b02613.
[9] H. Li, R.H. Yang, C.Y. Wang, Y.F. Wang, H. Chen, H.L. Zheng, et al., Corrosive behavior of silver electrode in inverted perovskite solar cells based on cu:nio, Ieee J Photovolt 9 (2019) 1081–1085, https://doi.org/10.1109/Jphotov.2019.2910192.
[10] H.Y. Zhang, H.X. Liu, W.B. Lu, W.X. Zhang, Y.N. Hao, P. Wang, et al., Analysis and suppression of metal-contact-induced degradation in inverted triple cation perovskite solar cells, Mater. Lett. 236 (2019) 736–738, https://doi.org/10.1016/j.matlet.2018.09.141.
[11] W.M. Qiu, M. Buffiére, G. Brammertz, U.W. Paetzold, L. Froyen, P. Heremans, et al., High efficiency perovskite solar cells using a PCBM/znO double electron transport layer and a short air-aging step, Org. Electron. 26 (2015) 30–35, https://doi.org/10.1016/j.orgel.2015.06.046.
[12] S. Svanström, A. García-Fernández, T.J. Jacobsson, I. Bidermane, T. Leitner, T. Sloboda, et al., The complex degradation mechanism of copper electrodes on lead halide perovskites, ACS Mater. Au 2 (2022) 301–312, https://doi.org/10.1021/acsmaterialsau.1c00038.
[13] L.F. Zhao, R.A. Kerner, Z.G. Xiao, Y.H.L. Lin, K.M. Lee, J. Schwartz, et al., Redox chemistry dominates the degradation and decomposition of metal halide perovskite optoelectronic devices, ACS Energy Lett. 1 (2016) 595–602, https://doi.org/10.1021/acsenergylett.6b00320.
[14] P.L. Qin, Q. He, G. Yang, X.L. Yu, L. Xiong, G.J. Fang, Metal ions diffusion at heterojunction chromium Oxide/CH3NH3PbI3 interface on the stability of perovskite solar cells, Surf. Interfaces 10 (2018) 93–99, https://doi.org/10.1016/j.surfin.2017.12.006.
[15] L.M. González, D. Ramirez, F. Jaramillo, Current status and trends of carbon-based electrodes for fully solution-processed perovskite solar cells, J. Energy Chem. 68 (2022) 222–246, https://doi.org/10.1016/j.jechem.2021.11.020.
[16] V. Ferguson, S.R.P. Silva, W. Zhang, Carbon materials in perovskite solar cells: prospects and future challenges, Energy Environ Mater 2 (2019) 107–118, https://doi.org/10.1002/eem2.12035.
[17] P. Pradid, K. Sanglee, N. Thongprong, S. Chuangchote, Carbon electrodes in perovskite photovoltaics, Materials 5989 (2021) 14, https://doi.org/10.3390/ma14205989.
[18] Y.Y. Yu, M.T. Hoang, Y. Yang, H.X. Wang, Critical assessment of carbon pastes for carbon electrode-based perovskite solar cells, Carbon 205 (2023) 270–293, https://doi.org/10.1016/j.carbon.2023.01.046.
[19] S. Zouhair, C. Clegg, I. Valitova, S. March, J.M. Jailani, V. Pecunia, Carbon electrodes for perovskite photovoltaics: interfacial properties, meta-analysis, and prospects, Sol. RRL 8 (2024), https://doi.org/10.1002/solr.202300929.
[20] W. Passatorntaschakorn, C. Bhoomanee, P. Ruankham, A. Gardchareon, P. Songsiriritthigul, D. Wongratanaphisan, Room-temperature carbon electrodes with ethanol solvent interlacing process for efficient and stable planar hybrid perovskite solar cells, Energy Rep. 7 (2021) 2493–2500, https://doi.org/10.1016/j.egyr.2021.04.031.
[21] Z.L. Ku, Y.G. Rong, M. Xu, T.F. Liu, H.W. Han, Full printable processed mesoscopic CH3NH3PbI3/TiO2 heterojunction solar cells with carbon counter electrode, Sci Rep-Uk 3132 (2013) 3, https://doi.org/10.1038/srep03132.
[22] X.Y. Liu, Z.Y. Liu, B. Sun, X.H. Tan, H.B. Ye, Y.X. Tu, et al., All low-temperature processed carbon-based planar heterojunction perovskite solar cells employing Mg-doped rutile TiO2 as electron transport layer, Electrochim. Acta 283 (2018) 1115–1124, https://doi.org/10.1016/j.electacta.2018.07.044.
[23] S.S. He, L.B. Qiu, D.Y. Son, Z.H. Liu, E.J. Juarez-Perez, L.K. Ono, et al., Carbon-based electrode engineering boosts the efficiency of all low-temperature processed perovskite solar cells, ACS Energy Lett. 4 (2019) 2032–2039, https://doi.org/10.1021/acsenergylett.9b01294.
[24] X.Y. Liu, X.H. Tan, Z.Y. Liu, H.B. Ye, B. Sun, T.L. Shi, et al., Boosting the efficiency of carbon-based planar CsPbBr3 perovskite solar cells by a modified multistep spin-coating technique and interface engineering, Nano Energy 56 (2019) 184–195, https://doi.org/10.1016/j.nanoen.2018.11.053.
[25] Z.Y. Liu, B. Sun, X.Y. Liu, J.H. Han, H.B. Ye, Y.X. Tu, et al., 15% efficient carbon based planar-heterojunction perovskite solar cells using a TiO2/SnO2 bilayer as the electron transport layer, J. Mater. Chem. A 6 (2018) 7409–7419, https://doi.org/10.1039/c8ta00526e.
[26] Z.Y. Liu, X.Y. Liu, B. Sun, X.H. Tan, H.B. Ye, Y.X. Tu, et al., Fully low-temperature processed carbon-based perovskite solar cells using thermally evaporated cadmium sulfide as efficient electron transport layer, Org. Electron. 74 (2019) 152–160, https://doi.org/10.1016/j.orgel.2019.07.004.
[27] J.J. Jin, M. Yang, W.Q. Deng, J. Xin, Q.D. Tai, J.W. Qian, et al., Highly efficient and stable carbon-based perovskite solar cells with the polymer hole transport layer, Sol. Energy 220 (2021) 491–497, https://doi.org/10.1016/j.solener.2021.03.081.
[28] F.G. Zhang, X.C. Yang, M. Cheng, W.H. Wang, L.C. Sun, Boosting the efficiency and the stability of low cost perovskite solar cells by using CuPc nanorods as hole transport material and carbon as counter electrode, Nano Energy 20 (2016) 108–116, https://doi.org/10.1016/j.nanoen.2015.11.034.
[29] Q.Q. Chu, B. Ding, J. Peng, H. Shen, X. Li, Y. Liu, et al., Highly stable carbon-based perovskite solar cell with a record efficiency of over 18% via hole transport engineering, J. Mater. Sci. Technol. 35 (2019) 987–993, https://doi.org/10.1016/j.jmst.2018.12.025.
[30] E. Widianto, Rosa ES. Shobih, K. Triyana, N.M. Nursam, I. Santoso, Graphene oxide as an effective hole transport material for low-cost carbon-based mesoscopic perovskite solar cells, Adv Nat Sci-Nanosci. 12 (2021) 035001, https://doi.org/10.1088/2043-6262/ac204a.
[31] M. Forouzandeh, M. Heidariramsheh, H.R. Heydarnezhad, H. Nikbakht, M. Stefanelli, L. Vesce, et al., Enhanced carbon-based back contact electrodes for perovskite solar cells: effect of carbon paste composition on performance and stability, Carbon 229 (2024) 119450, https://doi.org/10.1016/j.carbon.2024.119450.
[32] J. Sulistianto, A. Konno, T. Abuzairi, N.R. Poespawati, Effect of carbon electrode annealing temperature on the performance of n-i-p perovskite solar cells, Emergent Mater (2024), https://doi.org/10.1007/s42247-024-00798-8.
[33] Q. Luo, H. Ma, F. Hao, Q.Z. Hou, J. Ren, L.L. Wu, et al., Carbon nanotube based inverted flexible perovskite solar cells with all-inorganic charge contacts, Adv. Funct. Mater. 27 (2017) 1703068, https://doi.org/10.1002/adfm.201703068.
[34] I. Jeon, S. Seo, Y. Sato, C. Delacou, A. Anisimov, K. Suenaga, et al., Perovskite solar cells using carbon nanotubes both as cathode and as anode, J. Phys. Chem. C 121 (2017) 25743–25749, https://doi.org/10.1021/acs.jpcc.7b10334.
[35] Y. Zhou, X.W. Yin, Q. Luo, X.Y. Zhao, D.L. Zhou, J.H. Han, et al., Efficiently improving the stability of inverted perovskite solar cells by employing polyethylenimine-modified carbon nanotubes as electrodes, Acs Appl Mater Inter 10 (2018) 31384–31393, https://doi.org/10.1021/acsami.8b10253.
[36] V. Babu, R.F. Pineda, T. Ahmad, A.O. Alvarez, L.A. Castriotta, A. Di Carlo, et al., Improved stability of inverted and flexible perovskite solar cells with carbon electrode, Acs Appl Energ Mater 3 (2020) 5126–5134, https://doi.org/10.1021/acsaem.0c00702.
[37] T. Lukas, S. Seo, P. Holzhey, K. Stewart, C. Henderson, L. Wagner, et al., Charge extraction multilayers enable positive-intrinsic-negative perovskite solar cells with carbon electrodes, ACS Energy Lett. (2025) 2736–2742, https://doi.org/10.1021/acsenergylett.4c03403.

[38] C.O. Teixeira, L. Andrade, A. Mendes, Novel carbon-based material for perovskite solar cells back-contact, Int. J. Energy Res. 43 (2019) 7541–7546, https://doi.org/10.1002/er.4695.
[39] C.O. Teixeira, L. Andrade, A. Mendes, Easy processing carbon paper electrode for highly efficient perovskite solar cells, J. Power Sources 479 (2020) 229071v, https://doi.org/10.1016/j.jpowsour.2020.229071.
[40] M. Degani, Q. An, M. Albaladejo-Siguan, Y.J. Hofstetter, C. Cho, F. Paulus, et al., 23.7% efficient inverted perovskite solar cells by dual interfacial modification, Sci. Adv. 7 (2021) eabj7930, https://doi.org/10.1126/sciadv.abj7930.
[41] W.J. Yu, Y. Zou, S.N. Zhang, Z.S. Liu, C.C. Wu, B. Qu, et al., Carbon-based perovskite solar cells with electron and hole-transporting/-blocking layers, Mater Futures 2 (2023) 022101, https://doi.org/10.1088/2752-5724/acbbc2.
[42] I. Jeon, J. Yoon, N. Ahn, M. Atwa, C. Delacou, A. Anisimov, et al., Carbon nanotubes versus graphene as flexible transparent electrodes in inverted perovskite solar cells, J. Phys. Chem. Lett. 8 (2017) 5395–5401, https://doi.org/10.1021/acs.jpclett.7b02229.
[43] S.L. Hellstrom, M. Vosgueritchian, R.M. Stoltenberg, I. Irfan, M. Hammock, Y. B. Wang, et al., Strong and stable doping of carbon nanotubes and graphene by MoOx for transparent electrodes, Nano Lett. 12 (2012) 3574–3580, https://doi.org/10.1021/nl301207e.
[44] A. Kuruvila, P.R. Kidambi, J. Kling, J.B. Wagner, J. Robertson, S. Hofmann, et al., Organic light emitting diodes with environmentally and thermally stable doped graphene electrodes, J. Mater. Chem. C 2 (2014) 6940–6945, https://doi.org/10.1039/c4tc01224k.
[45] I. Jeon, C. Delacou, A. Kaskela, E.I. Kauppinen, S. Maruyama, Y. Matsuo, Metal-electrode-free window-like organic solar cells with p-Doped carbon nanotube thin-film electrodes, Sci Rep-Uk 31348 (2016) 6, https://doi.org/10.1038/srep31348.
[46] I. Jeong, H.J. Kim, B.S. Lee, H.J. Son, J.Y. Kim, D.K. Lee, et al., Highly efficient perovskite solar cells based on mechanically durable molybdenum cathode, Nano Energy 17 (2015) 131–139, https://doi.org/10.1016/j.nanoen.2015.07.025.
[47] Y.X. Zhao, A.M. Nardes, K. Zhu, Effective hole extraction using MoOx-Al contact in perovskite CH3NH3PbI3 solar cells, Appl. Phys. Lett. 104 (2014) 213906, https://doi.org/10.1063/1.4880899.
[48] D.M. Torres-Herrera, P.M. Moreno-Romero, D. Cabrera-German, H.J. Cortina-Marrero, M. Sotelo-Lerma, H.L. Hu, Thermal co-evaporated moox:au thin films and its application as anode modifier in perovskite solar cells, Sol. Energy 206 (2020) 136–144, https://doi.org/10.1016/j.solener.2020.05.105.
[49] E.M. Sanehira, B.J.T. de Villers, P. Schulz, M.O. Reese, S. Ferrere, K. Zhu, et al., Influence of electrode interfaces on the stability of perovskite solar cells: reduced degradation using MoOx/Al for hole collection, ACS Energy Lett. 1 (2016) 38–45, https://doi.org/10.1021/acsenergylett.6b00013.
[50] S. Madani, T. Tesfamichael, N. Motta, H.X. Wang, Simulation of perovskite solar cells using molybdenum oxide thin films as interfacial layer for enhancing device performance, Sustain. Mater. Technol. 32 (2022) e00426, https://doi.org/10.1016/j.susmat.2022.e00426.
[51] Z.Y. Jiang, M. Pan, F.M. Ren, R. Chen, Z.X. Sun, Z.C. Yang, et al., Boosting stability of inverted perovskite solar cells with magnetron-sputtered molybdenum rear electrodes, Rare Met. 42 (2023) 3741–3754, https://doi.org/10.1007/s12598-023-02426-6.
[52] P. Gebhardt, S. Hoffmann, T. Wenzel, L. Friedrich, S. Herceg, D.M. Subasi, et al., Lead-free PV modules: industrial realization and evaluation of environmental impact, in: WCPEC-8, 2022, pp. 930–934. Milano, Italy.
[53] Y. Teng, X.D. Wang, H.Y. Chen, J.F. Liao, W.G. Li, D.B. Kuang, Iron-assisted engineering of molybdenum phosphide nanowires on carbon cloth for efficient hydrogen evolution in a wide pH range, J. Mater. Chem. A 5 (2017) 22790–22796, https://doi.org/10.1039/c7ta07895a.
[54] J. Swiatowska-Mrowiecka, S. de Diesbach, V. Maurice, S. Zanna, L. Klein, E. Briand, et al., Li-ion intercalation in thermal oxide thin films of MoO as studied by XPS, RBS, and NRA, J. Phys. Chem. C 112 (2008) 11050–11058, https://doi.org/10.1021/jp800147f.
[55] M.P. Casaletto, A. Longo, A. Martorana, A. Prestianni, A.M. Venezia, XPS study of supported gold catalysts: the role of Au0 and Au+δ species as active sites, Surf. Interface Anal. 38 (2006) 215–218, https://doi.org/10.1002/sia.2180.
[56] Y.S. Pestovsky, T. Srichana, Formation of aggregate-free gold nanoparticles in the cyclodextrin-tetrachloroaurate system follows finke-watzky kinetics, Nanomaterials-Basel 12 (2022) 583, https://doi.org/10.3390/nano12040583.
[57] Ossila, PTAA for perovskite applications. https://www.ossila.com/products/ptaa-perovskites?_pos=1&_sid=fd4fafbbd&_ss=r, 2025. September 2025.
[58] X.P. Zheng, Y. Hou, C.X. Bao, J. Yin, F.L. Yuan, Z.R. Huang, et al., Managing grains and interfaces via ligand anchoring enables 22.3%-efficiency inverted perovskite solar cells, Nat. Energy 5 (2020) 131–140, https://doi.org/10.1038/s41560-019-0538-4.
[59] Ossila. PCBM. https://www.ossila.com/products/pcbm, 2025. September 2025.
[60] Q. Zhao, R.S. Wu, Z.L. Zhang, J. Xiong, Z. He, B.J. Fan, et al., Achieving efficient inverted planar perovskite solar cells with nondoped PTAA as a hole transport layer, Org. Electron. 71 (2019) 106–112, https://doi.org/10.1016/j.orgel.2019.05.019.
[61] International Organization for Standardization, ISO 14040: Environmental Management - Life Cycle Assessment - Principles and Framework, 2006.
[62] International Organization for Standardization, ISO 14044: Life Cycle Assessment - Requirements and Guidelines, 2006.
[63] M.A.J. Huijbregts, Z.J.N. Steinmann, P.M.F. Elshout, G. Stam, F. Verones, M. Vieira, et al., ReCiPe2016: a harmonised life cycle impact assessment method at midpoint and endpoint level, Int. J. Life Cycle Assess. 22 (2017) 138–147, https://doi.org/10.1007/s11367-016-1246-y.
[64] M.A.J. Huijbregts, Z.J.N. Steinmann, P.M.F. Elshout, G. Stam, F. Verones, M. Vieira, et al., Recipe 2016: a Harmonized Life Cycle Impact Assessment Method at Midpoint and Endpoint Level - Report I: Characterization, National Institute for Public Health and the Environment, The Netherlands, 2016.
[65] L. Usai, C.R. Hung, F. Vásquez, M. Windsheimer, O.S. Burheim, A.H. Stromman, Life cycle assessment of fuel cell systems for light duty vehicles, current state-of-the-art and future impacts, J. Clean. Prod. 280 (2021) 125086, https://doi.org/10.1016/j.jclepro.2020.125086.